8-12-2023

Whistler-Mode Waves in Magnetic Ducts

Anatoly V. Streltsov
Embry Riddle Aeronautical University, streltsa@erau.edu

Salman A. Nejad
Embry-Riddle Aeronautical University

Whistler-Mode Waves in Magnetic Ducts

Anatoly V. Streltsov and Salman A. Nejad

Department of Physical Sciences, Embry-Riddle Aeronautical University, Daytona Beach, Florida, USA

Key Points:

- MMS satellites observe ELF whistler-mode waves inside small-scale irregularities of the magnetic field.
- We provide theoretical criteria for the wave to be trapped by the field-aligned magnetic irregularities.
- We model ducting of the observed waves and identify parallel and perpendicular wavenumbers providing ducting of these waves.

Corresponding author: A.V. Streltsov, `streltsa@erau.edu`

Abstract

Observations from the NASA MMS satellites show packages of ELF whistler-mode waves localized inside the small-scale irregularities of the magnetic field. These irregularities are formed by the narrow field-aligned channels where the magnitude of the background magnetic field inside the channel is greater or less than outside. By analogy with the classical density ducts, we introduce the high-B duct (HBD), where the magnitude of the field inside the channel is greater than the outside, and the low-B duct (LBD), where the magnitude of the field inside the channel is less than the outside. We investigate the guiding of the ELF whistler-mode waves by high-B and low-B ducts. We derive the analytical criteria for the wave ducting by these ducts and confirm them with two-dimension, time-dependent simulations of the electron-MHD model. Also, we model ELF whistler-mode waves observed inside the high-B and low-B ducts by MMS satellites.

1 Introduction

Extremely-low frequency (300 Hz - 3 kHz) whistler-mode waves have garnered significant attention from the space plasma community [*Katoh*, 2014; *Xu et al.*, 2020; *Hosseini et al.*, 2021] due to their capacity to engage in cyclotron resonance with high-energy electrons (with energies of several 100 keV and higher) in the Earth's radiation belt [*Nunn*, 1974; *Trakhtengerts et al.*, 2003; *Omura and Summers*, 2006]. These interactions alter the pitch angle of energetic particles, leading to their precipitation from the magnetosphere. Therefore, a controlled injection of whistler-mode waves from Earth or space into the magnetosphere can mitigate the presence of energetic particles in the Earth's radiation belt and make the environment safer for electronics and crews on space platforms [*Inan et al.*, 1985, 2003].

Whistler-mode waves can be guided along the ambient magnetic field by the field-aligned density irregularities, known as ducts. These ducts can be formed by the density depletion (low-density duct or LDD), enhancement (high-density duct or HDD), shelf-like density structures, and single density gradient [*Zudin et al.*, 2019; *Streltsov*, 2021a,b]. The ducting of the whistler-mode waves explain their propagation in the Earth's magnetosphere over a significant distance (like from one hemisphere to another) with a little attenuation.

Various aspects of the guiding of the whistler-mode waves by different density structures have been studied in the space and laboratory plasma by a great number of authors [*Storey*, 1954; *Nunn*, 1974; *Karpman et al.*, 1974; *Stenzel*, 1976; *Omura et al.*, 1991; *Trakhtengerts et al.*, 1996; *Nunn and Smith*, 1996; *Stenzel*, 1999; *Trakhtengerts et al.*, 1996; *Nunn and Smith*, 1996; *Hobara et al.*, 2000; *Kostrov et al.*, 2000]. The basic physics of these processes is described in the monographs by *Helliwell* [1965], *Sazhin* [1993], and *Kondrat'ev et al.* [1999].

This study focuses on the guiding of the whistler-mode waves by the field-aligned inhomogeneities of the background magnetic field. These inhomogeneities can be formed by the localized increase and decrease of the magnitude of the background magnetic field. By the analogy with the ducts formed by the field-aligned increases and decreases of the plasma density, it is reasonable to call these magnetic structures high-B ducts and low-B ducts, or HBD and LBD.

High-B ducts can be produced, for example, by the the depolarizing flux bundles (DFBs), carrying particles and magnetic fields from the magnetotail to the inner magnetosphere during substorms [*Birn et al.*, 2012; *Liu et al.*, 2013; *Runov et al.*, 2009; *Sitnov et al.*, 2009]. Low-B ducts can be produced by the diamagnetic motion of freshly injected plasmas from the magnetotail [*He et al.*, 2017; *Huang et al.*, 2021; *Yin et al.*, 2021]. Also, the positive gradient portion of DFBs, along with the intrinsic dipole magnetic field of the terrestrial magnetosphere or the negative gradient portion of adjacent DFBs, can create a magnetic dip in the radial direction [*Artemyev et al.*, 2022; *Gabrielse et al.*, 2016; *Malykhin et al.*, 2021; *Zhou et al.*, 2009].

Despite the abundant presence of magnetic structures in the inner magnetosphere, the trapping mechanism of the whistler-mode waves by them has not been studied well. Recently, *Yu and Yuan* [2022] studied ducting of the whistler-mode wave by the magnetic dips and peaks by analyzing the wave refractive index.

In our approach, we use the whistler-mode dispersion relation to get the analytical criteria for the wave trapping in HBD and LBD. This approach let us identify the thresholds in magnitude of the ambient magnetic field providing trapping of the wave with some known frequency. It also allowed us to identify the ranges of the parallel and perpendicular wavelengths of the waves trapped in these ducts. We confirm the validity of this approach with two-dimensional, time-dependent simulations of the electron-

MHD model describing whistler-mode waves in the inhomogeneous plasma and the magnetic field. We also use this approach and simulations to model two events observed by the MMS satellites.

2 Observations

Observations by the NASA MMS satellites in the equatorial magnetosphere reveal localized packages of the whistler-mode waves that correlate with inhomogeneities of the background magnetic field.

Figure 1 shows two events consisting of the localized packages of ELF waves and magnetic inhomogeneities observed by the MMS1 satellite in the equatorial dawnside magnetosphere on March 6, 2016. Figure 2 shows the location and the trajectory of the MMS satellites in the X-Y plane in GSE coordinates on March 6, 2016. The electron number density is obtained by the MMS1 FPI/DES instrument, the power spectral density of the electric field is provided by the FIELDS Instrument Suite [*Torbert et al.*, 2016], and the magnetic field is provided by the MMS1 Flux-Gate Magnetometer(FGM) [*Russell et al.*, 2016].

- **Event I.** The first event consists of the whistler-mode waves in the high-B Duct observed from 19:38:58 to 19:39:04 UT. Figure 1a shows with a color palette the power spectral density (PSD) of the x-component of the electric field (in the GSE coordinate system) in the frequency range 300-500 Hz and the magnitude of the background magnetic field (white line). Figure 1b shows the corresponding electron density. The maximum magnitude of the ambient magnetic field inside the duct is 74.16 nT (here the electron cyclotron frequency $\omega_{ce} = 13.03 \times 10^3$ rad/s and the lower hybrid frequency $\omega_{LH} = 3.04 \times 10^2$ rad/s), and it changes during this time interval by ≈21.38 nT or 28.8% compared to the minimum values outside the duct of 52.87 nT. For comparison, during this time interval, the electron density changes from 67 cm^{-3} to 70 cm^{-3}, or by 4.5%. The density inside the duct is 67.7 cm^{-3} ($\omega_{pe} = 4.63 \times 10^5$ rad/s). The frequency of the wave in the duct is 400 Hz, and the width of the duct is ≈5.78 km.
- **Event II.** The second event consists of the whistler-mode wave in the low-B Duct observed from 18:36:58 to 18:37:09 UT. Figures 1c shows the power spectral density of E_x in the frequency range 110–370 Hz (with the color palette) and the mag-

nitude of the ambient magnetic field (with the white line). The minimum magnitude of the ambient magnetic field inside the duct is 45.2 nT ($\omega_{ce} = 7.95 \times 10^3$ rad/s, $\omega_{LH} = 1.85 \times 10^2$ rad/s). The field changes during this time interval from minimum to the maximum value of 66.5 nT by 21.3 nT or 47.2%. The electron density inside the duct is 75.4 cm^{-3} ($\omega_{pe} = 4.98 \times 10^5$ rad/s), and it changes during this time interval by 4.1 cm^{-3}, or 5.4%. The frequency of the wave in the duct is 272 Hz, and the width of the duct is ≈22.7 km.

In the next section, we present an analytical investigation of the physical mechanisms providing ducting of the whistler-mode waves by the field-aligned magnetic irregularities. Our approach is based on the analysis of the dispersion relation for whistler-mode waves, and it is similar to the analysis of the wave-guiding by the density ducts developed earlier by *Streltsov et al.* [2006].

3 Model

The whistler-mode waves in the magnetosphere can be described with a so-called quasi-longitudinal approximation of the electron-MHD (EMHD) model. This model assumes that the ions are immobile and the electrons can be treated as the cold fluid carrying the current [*Helliwell*, 1965; *Gordeev et al.*, 1994]. The immobility of the ions means that $\omega_{LH} < \omega$, where ω_{LH} is the lower hybrid frequency and ω is the angular frequency of the wave.

Because the plasma is quasi-neutral and the ions are immobile, the model consists of the electron momentum equation and the Maxwell equations only. The quasi-longitudinal approximation means that the displacement current is omitted in the Ampere's law. This assumption significantly simplifies the analytical and numerical treatment of the considered problem, but it is valid only if $\omega < \omega_{ce} \ll \omega_{pe}$ [*Sazhin*, 1993]. Thus, the ELF whistler-mode waves can be described with the quasi-longitudinal approximation of EMHD if

$$\omega_{LH} < \omega < \omega_{ce} \ll \omega_{pe} \tag{1}$$

It should be mentioned here that the conditions (1) are satisfied for the parameters of the wave, plasma, and the magnetic field observed during Event I and Event II.

The dispersion relation of whistler-mode waves derived from the linearized quasi-longitudinal EMHD in the homogeneous media is

$$k^2 - \frac{\omega_{ce}}{\omega} k_{\|} k + \frac{1}{\lambda_e^2} = 0. \tag{2}$$

Here, $k_{\|}$ and $k_{\perp}$ are parallel and perpendicular to $\mathbf{B}_0$ wavenumber, $k^2 = k_{\|}^2 + k_{\perp}^2$, and $\lambda_e = c/\omega_{pe}$ is the electron plasma skin depth.

Relation (2) can be used to express B in terms of ω, $k_{\perp}$, $k_{\|}$, and ω_{pe} in the form

$$B = \frac{\omega}{k_{\|}} \frac{m_e}{e} \left(k + \frac{1}{k\lambda_e^2} \right). \tag{3}$$

Figure 3a shows the plot of B as a function of $k_{\perp}$ for $\omega = 1.71 \times 10^3$ rad/s ($f = 272$ Hz), $k_{\|} = 0.7$ rad/km ($\lambda_{\|} = 8.98$ km), and $\omega_{pe} = 4.98 \times 10^5$ rad/s ($n = 78$ cm^{-3}). These parameters of the wave and the media are similar to those observed by MMS1 during Event II.

Figure 3 shows that there are two different real $k_{\perp}$ if $B_2 < B < B_1$, one real $k_{\perp}$ if $B > B_1$, and there is no real $k_{\perp}$ if $B < B_2$. Here,

$$B_1 = \omega \frac{m_e}{e} \left(1 + \frac{1}{k_{\|}^2 \lambda_e^2} \right), \tag{4}$$

$$B_2 = \omega \frac{m_e}{e} \left(\frac{2}{k_{\|} \lambda_e} \right). \tag{5}$$

The general formula for $k_{\perp}$ can be obtained in the following way. First, use (5) to express $k_{\|}$ as

$$k_{\|} = \omega \frac{m_e}{e} \frac{1}{B_2} \frac{2}{\lambda_e} = \frac{\omega}{\omega_{ce}} \frac{B}{B_2} \frac{2}{\lambda_e}. \tag{6}$$

Next, put (6) into (2)

$$k^2 - \frac{B}{B_2} \frac{2}{\lambda_e} k + \frac{1}{\lambda_e^2} = 0, \tag{7}$$

solve (7) for k

$$k_{1,2} = \frac{B}{B_2} \frac{1}{\lambda_e} \left(1 \mp \sqrt{1 - \frac{B_2^2}{B^2}} \right) = k_{\|} \frac{\omega_{ce}}{2\omega} \left(1 \mp \sqrt{1 - \frac{B_2^2}{B^2}} \right), \tag{8}$$

take (8) to the second power and remember that $k^2 = k_{\|}^2 + k_{\perp}^2$

$$k_{\|}^2 + k_{\perp_{1,2}}^2 = k_{\|}^2 \frac{\omega_{ce}^2}{4\omega^2} \left(1 \mp \sqrt{1 - \frac{B_2^2}{B^2}} \right)^2. \tag{9}$$

Finally,

$$k_{\perp_{1,2}} = k_{\|} \left[\frac{\omega_{ce}^2}{4\omega^2} \left(1 \mp \sqrt{1 - \frac{B_2^2}{B^2}} \right)^2 - 1 \right]^{1/2}. \tag{10}$$

These results explain the main concept of wave trapping by the low-B and high-B ducts illustrated in Figure 3b. Namely, if B_I is the magnetic field inside the duct, and B_L is the magnetic field outside the low-B duct, then the following condition should be satisfied for a low-B duct to guide the wave

$$B_2 < B_I < B_1 < B_L \tag{11}$$

The conditions for the wave to be trapped in the high-B duct is

$$B_H < B_2 < B_I < B_1, \tag{12}$$

where B_H is the magnitude of the field outside the high-B duct.

Figure 3a also shows an important difference between the ducting of whistler-mode waves by LBD and HBD. Namely, if $B_2 < B < B_1$ inside the duct, then there are two whistler-mode waves with the same ω and $k_\parallel$ but different $k_\perp$. In the case of LBD, for any magnetic field outside the duct $B_L > B_1$ there always exists a wave with the same ω and $k_\parallel$ as the wave inside the duct. This wave can couple to the waves propagating inside the LBD and carry the wave energy away from the duct, resulting in the leakage of the electromagnetic energy from LBD.

For the HBD, the situation is different. Since there are no waves with a real $k_\perp$ and the same ω and $k_\parallel$ outside the HBD, where $B_H < B_2$, the inner waves cannot couple to waves propagating outside the duct, and hence, we expect that there is no leakage from HBD.

These features of the low-B and high-B ducts are in contrast with the properties of the ducts formed by the field-aligned density irregularities. Namely, the high-density duct (HDD) leaks electromagnetic energy due to the coupling with the wave outside the duct, and the low-density duct (LDD) is leak-free [*Streltsov et al.*, 2006; *Streltsov*, 2021a].

The criteria for ducting of the whistler-mode waves given by the expressions (11) and (12) are obtained from the dispersion relation (2) derived in the homogeneous media. The media are certainly not homogeneous when the ducting is considered. Therefore, these criteria need to be verified with the numerical solution of the full set of EMHD equations in the realistically inhomogemeous plasma and the magnetic field. These simulations are described in the next section.

4 Simulations

The quasi-longitudinal electron-MHD model used in this paper consists of three vector equations for **E**, **B**, and the electron velocity **v** (e.g., [*Streltsov et al.*, 2006]).

$$\frac{m_e}{\mu_0 n_e e^2}\nabla\times\nabla\times\mathbf{E}+\mathbf{E}=-\frac{m_e}{e}(\mathbf{v}\cdot\nabla)\mathbf{v}-\mathbf{v}\times\mathbf{B}, \tag{13}$$

$$\frac{\partial\mathbf{B}}{\partial t}=-\nabla\times\mathbf{E}, \tag{14}$$

$$\frac{\partial\mathbf{v}}{\partial t}=\frac{1}{\mu_0 n_e e}\nabla\times\nabla\times\mathbf{E}. \tag{15}$$

These equations are implemented numerically using the finite-difference, time-domain (FDTD) technique in a two-dimensional rectangular domain (x, z). All spatial derivatives are approximated with the forth-order finite differences. Equation (13) for **E** is solved at every time step by the method of successive over-relaxation (SOR). To advance the model in time, a third-order predictor-corrector algorithm is used, with the Adamse-Bashforth method serving as a predictor and the Adamse-Moulton method serving as a corrector.

The background magnetic field is pointed in the z-direction. The plasma density and the background magnetic field are homogeneous in the z-direction and inhomogeneous in the x-direction. The size of the domain in the z-direction is l_z (from $-l_z/2$ to $l_z/2$), and the size in the x-direction is l_x (from $-l_x/2$ to $l_x/2$).

The boundary conditions for all variables in the z-direction are periodic: $\mathbf{E}\ (t,\ x,\ -l_z/2) = \mathbf{E}\ (t,\ x,\ l_z/2)$, $\mathbf{B}\ (t,\ x,\ -l_z/2) = \mathbf{B}\ (t,\ x,\ l_z/2)$, and $\mathbf{v}\ (t,\ x,\ -l_z/2) = \mathbf{v}\ (t,\ x,\ l_z/2)$. The size of the computational domain in the z-direction, l_z, is set equal to one $\lambda_\parallel$. The boundary conditions in the x-direction are of the Dirichlet type: $\mathbf{E}\ (t,\ -l_x/2,\ z) = \mathbf{E}\ (t,\ l_x/2,\ z) \equiv 0$, $\mathbf{B}\ (t,\ -l_x/2,\ z) = \mathbf{B}\ (t,\ l_x/2,\ z) \equiv 0$, $\mathbf{v}\ (t,\ -l_x/2,\ z) = \mathbf{v}\ (t,\ l_x/2,\ z) \equiv 0$. The initial conditions for **E**, **B**, and **v**, as well as other details of the code are described in *Streltsov et al.* [2006].

4.1 Low-B Duct

We start the verification of the ducting criteria (11) and (12) by simulating the dynamics of the whistler-mode waves in the model low-B duct. We assume that the plasma density is homogeneous in the x and z directions and $n = 75.4$ cm^{-3}. The magnetic field is homogeneous in the z-direction and inhomogeneous in x. The magnitude of the magnetic field inside the duct is $B_I = 45.4$ nT and outside $B_L = 66$ nT. The width of the duct is 22 km.

The frequency of the wave is f = 272 Hz, and the parallel wavelength is $\lambda_{\|}$ = 7.70 km. For these parameters of the wave and plasma, relations (4) and (10) provide B_1 = 48.6 nT, B_2 = 38.9 nT, $k_{\perp_1}$ = 0.43 rad/km ($\lambda_{\perp_1}$ = 14.46 km), and $k_{\perp_2}$ = 2.77 rad/km ($\lambda_{\perp_2}$ = 2.27 km).

Figures 4a, 4a', and 4a" show results from the simulations of this wave during time interval of 368 ms or 100 wave periods. Figure 4a shows the dynamic of E_x (x, z = 0, t). The results are presented in (x-t) domain because the media is assumed to be homogeneus in z-direction, the code uses periodic boundary conditions in the z-direction, and the size of the domain in the z-direction is set equal to one $\lambda_{\|}$. Figure 4a' shows the profile of B_0 across $\mathbf{B}_0$, and Figure 4a" shows the dynamic of E_x in the center of the computational domain, E_x (x = 0, z = 0, t).

For comparison, Figure 4b shows the dynamic of E_x (x, z = 0, t) of the same wave in the simulation with a homogeneous background magnetic field (B = 45.4 nT) and plasma density (n = 75.4 cm^{-3}). The profile of B_0 across $\mathbf{B}_0$ is shown in Figure 4b', and the dynamic of E_x (x = 0, z = 0, t), is shown in Figure 4b".

The main conclusion from the results shown in Figure 4 is that the wave with this particular ω and $\lambda_{\|}$ is indeed trapped inside the low-B duct in strict accordance with the prediction based on the analytical criteria (11). Figure 4b confirms that the ducting occurs due to the inhomogeneity in the background magnetic field, because without that inhomogeneity, the same wave propagates under a large angle to the magnetic field.

4.2 High-B Duct

Next, we consider propagation of the whistler-mode wave in the high-B duct. Again, we assume that the plasma density is homogeneous in the x and z directions and n = 68 cm^{-3}. The magnetic field is homogeneous in z-direction and inhomogeneous in x. The magnitude of the magnetic field inside the duct is B_I = 74.0 nT and outside B_H = 53 nT. The width of the duct is 29 km.

The frequency of the wave is f = 410 Hz and the parallel wavelength is $\lambda_{\|}$ = 9.26 km. For these parameters of the wave and plasma, relations (4)-(6) provide B_1 = 91.4 nT, B_2 = 67.1 nT, $k_{\perp_1}$ = 0.725 rad/km ($\lambda_{\perp_1}$ = 8.66 km), and $k_{\perp_2}$ = 2.33 rad/km ($\lambda_{\perp_2}$ = 2.70 km).

Figures 5a, 5a', and 5a" show results from the simulations of this wave during the time interval of 368 ms or 100 wave periods. Figure 5a shows the dynamic of E_x (x, $z = 0$, t), Figure 5a' shows the profile of B_0 across $\mathbf{B}_0$, and Figure 5a" shows the dynamic of E_x in the center of the computational domain, E_x ($x = 0$, $z = 0$, t).

For comparison, Figure 5b shows the dynamic of E_x (x, $z = 0$, t) of the same wave in the simulation with a homogeneous background magnetic field (B = 74.0 nT) and plasma density (n = 68.0 cm^{-3}). The profile of B_0 across $\mathbf{B}_0$ is shown in Figure 5b', and the dynamic of E_x ($x = 0$, $z = 0$, t), is shown in Figure 5b".

The main conclusion from the results shown in Figure 5 is that the high-B duct indeed traps and guides the wave with these particular ω and $\lambda_{\|}$ as it is predicted by the analytical criteria (12). Figure 5b confirms that the ducting occurs due to the inhomogeneity in the background magnetic field, because without that inhomogeneity, the same wave propagates under a large angle to the magnetic field.

Now, after the criteria for the whistler-mode wave ducting with the low-B duct and high-B duct are verified with rigorous numerical simulations, we will apply the developed formalism for modeling events observed by the MMS1 satellite on March 6, 2016.

4.3 Event I

Event I consists of the whistler-mode waves trapped inside the high-B duct. We assume that the plasma density and the background magnetic field are homogeneous in the z-direction, and both are inhomogeneous in the x-direction. The amplitudes of n and B_0 inside the duct, as well as the width of the duct, are taken from the observations shown in Figure 1a and 1b. The frequency of the wave is 400 Hz. The initial conditions for the wave used in the simulation are calculated assuming that $\lambda_{\|}$ = 10.5 km, n_0 = 67.6 cm^{-3}, and B_0 = 74.2 nT, which is the maximum value of the magnetic field inside the duct. For these parameters of the wave and plasma, relations (4), (5), and (10) provide B_1 = 109.3 nT, B_2 = 73.7 nT, $k_{\perp_1}$ = 0.725 rad/km ($\lambda_{\perp_1}$ = 8.66 km), and $k_{\perp_2}$ = 2.33 rad/km ($\lambda_{\perp_2}$ = 2.70 km).

Figures 6a, 6a', and 6a" show results from the simulations of this wave during the time interval of 250 ms or 100 wave periods. Figure 6a shows the dynamic of E_x (x, z

$= 0$, t), Figure 6a' shows the profile of B_0 across $\mathbf{B}_0$, and Figure 6a" shows the dynamic of E_x in the center of the computational domain, E_x ($x = 0$, $z = 0$, t).

For comparison, Figure 6b shows the dynamic of E_x (x, $z = 0$, t) of the same wave in the simulation with a homogeneous background magnetic field ($B = 74.2$ nT). The profile of B_0 across $\mathbf{B}_0$ is shown in Figure 6b', and the dynamic of E_x ($x = 0$, $z = 0$, t), is shown in Figure 6b". In this simulation, the background plasma density is the same as in the simulation illustrated in Figure 6a.

The main conclusion from the results shown in Figure 6 is that the observations conducted by the MMS1 satellite in the dawn-side magnetosphere on March 6, 2016 indeed demonstrate the whistler-mode wave inside the high-B duct. Figure 6b confirms that the ducting occurs due to the inhomogeneity in the background magnetic field, because without that inhomogeneity, this wave propagates under a large angle to the ambient magnetic field.

4.4 Event II

Event II consists of the whistler-mode waves trapped inside the low-B duct. To model this event, we again assume that the plasma density and the background magnetic field are homogeneous in the z-direction and inhomogeneous in the x-direction. The amplitudes of n and B_0 inside the duct, as well as the width of the duct, are taken from the observations shown in Figure 1c and 1d. The frequency of the wave is 272 Hz. The initial conditions for the wave used in the simulation are calculated assuming that $\lambda_{\parallel} = 7.60$ km, $n_0 = 78.1$ cm^{-3}, and $B_0 = 45.20$ nT, which is the minimal value of the magnetic field inside the duct. For these parameters of the wave and plasma, relations (4), (5), and (10) provide $B_1 = 49$ nT, $B_2 = 39$ nT, $k_{\perp_1} = 0.482$ rad/km ($\lambda_{\perp_1} = 13.03$ km) and $k_{\perp_2} = 2.77$ rad/km ($\lambda_{\perp_2} = 2.26$ km).

Figures 7a, 7a', and 7a" show results from the simulations of this wave during the time interval of 368 ms or 100 wave periods. Figure 6a shows the dynamic of E_x (x, z $= 0$, t), Figure 6a' shows the profile of B_0 across $\mathbf{B}_0$, and Figure 7a" shows the dynamic of E_x in the center of the computational domain, E_x ($x = 0$, $z = 0$, t).

For comparison, Figure 7b shows the dynamics of E_x (x, $z = 0$, t) of the same wave in the simulation with a homogeneous background magnetic field ($B = 45.20$ nT). The profile of B_0 across $\mathbf{B}_0$ is shown in Figure 7b', and the dynamic of E_x $(x = 0,\, z = 0,\, t)$, is shown in Figure 7b". In this simulation, the background plasma density is the same as in the simulation illustrated in Figure 7a.

The main conclusion from the results shown in Figure 7 is that the observations conducted by the MMS1 satellite in the dawn-side magnetosphere on March 6, 2016 indeed demonstrate the whistler-mode wave inside the low-B duct. Figure 7b confirms that the ducting occurs due to the inhomogeneity in the background magnetic field, because without that inhomogeneity, this wave propagates under a large angle to the ambient magnetic field.

5 Conclusions

The paper presents results from the analytical and numerical study of the propagation of ELF whistler-mode waves in the localized field-aligned irregularities of the ambient magnetic field. This study is motivated by the observations performed by NASA MMS satellites in the dawn-side equatorial magnetosphere, which reveal packages of whistler-mode waves localized inside small-scale regions where the magnitude of the magnetic field was decreased or increased. We call these regions low-B ducts and high-B ducts, correspondingly.

By analogy with our previous investigations of the whistler-mode waves in the high-density and low-density ducts, this study is based on the analysis on the dispersion relation derived from the linearized equations of the quasi-longitudinal EMHD model. We provide analytical criteria for whistler-mode waves to be trapped in the low-B and high-B ducts. The validity of these criteria is confirmed with two-dimensional, time-dependent simulations of the complete set of EMHD equations in the inhomogeneous plasma and the magnetic field.

Our analysis demonstrates that the low-B duct can leak energy outside due to the potential coupling between the waves propagating inside and outside of the duct channel. The high-B duct is "leak-free" because there is no wave with the same frequency and the parallel wavelength propagating outside the duct. These properties of the magnetic ducts are opposite to the properties of density ducts. There, the high-density duct can leak electromagnetic energy due to coupling with the waves outside the channel, and the low-density duct is "leak-free."

Finally, we perform numerical simulations of two observational events recorded by the MMS1 satellite on March 6, 2016, where the whistler-mode waves were detected inside the low-B and high-B ducts. Simulations demonstrate that these waves are indeed ducted by the field-aligned inhomogeneities of the magnetic field, and without these inhomogeneities, the wave propagates under large angle to the magnetic field.

The main conclusion from our study is that the magnetic ducts formed by the localized field-aligned enhancements and depletions of the magnetic field can guide whistler-mode waves over significant distances in the magnetosphere with a little attenuation. In full analogy with the ducts formed by the field-aligned density irregularities, magnetic ducts are defined by thresholds depending on the wave frequency, parallel wavelength, and magnitude of the plasma density.

Acknowledgments

This research was supported by the Air Force Office of Sponsored Research Grants FA9453-21-2-0039.

Data Availability

The MMS data used in this study are available from https://lasp.colorado.edu/mms/sdc/public/datasets/ and https://cdaweb.gsfc.nasa.gov/. The Linux executable code (r1000), data files used to run the code (rbsp_dat_newN.dat and Dens_Bfield_In.dat), and the results from the simulations (ExfieldS.dat) shown in Figures 4, 5, 6, and 7 are available from https://doi.org/10.6084/m9.figshare.2

References

Artemyev, A. V., A. I. Neishtadt, and V. Angelopoulos (2022), On the role of whistler-mode waves in electron interaction with dipolarizing flux bundles, *J. Geophys. Res.: Space Phys.*, *127*.

Birn, J., A. V. Artemyev, D. N. Baker, M. Echim, M. Hoshino, and L. M. Zelenyi (2012), Particle acceleration in the magnetotail and aurora, *Space Science Rev.*, *173*, 49.

Gabrielse, C., C. Harris, V. Angelopoulos, A. Artemyev, and A. Runov (2016), The role of localized inductive electric fields in electron injections around dipolarizing flux bundles, *J. of Geophys. Res.: Space Phys.*, *121*(4), 9560–9585.

Gordeev, A., A. Kingsep, and L. Rudakov (1994), Electron magnetohydrodynamics, *Physics Reports*, *243*, 215–315.

He, Z., L. Chen, H. Zhu, Z. Xia, G. D. Reeves, Y. Xiong, and Y. Cao (2017), Multiple-satellite observation of magnetic dip event during the substorm on 10 october 2013, *Geophys. Res. Lett*, *44*, 9167.

Helliwell, R. (1965), *Whistlers and Related Ionospheric Phenomena*, Stanford University Press, Stanford.

Hobara, Y., V. Y. Trakhtengerts, A. G. Demekhov, and M. Hayakawa (2000), Formation of electron beams by interaction of a whistler wave packet with radiation belt electrons, *J. Atmos. Sol.-Terr. Phys.*, *62*, 541.

Hosseini, P., O. Agapitov, V. Harid, and M. Gołkowski (2021), Evidence of small scale plasma irregularity effects on whistler mode chorus propagation., *Geophys. Res. Lett.*, *48*, e2021GL092,850, doi:10.1029/2021GL092850.

Huang, Z., Z. Yuan, X. Yu, Z. Xue, and Z. Ouyang (2021), Simultaneous generation of emic and ms waves during the magnetic dip in the inner magnetosphere, *Geophys. Res. Lett*, *48*, e2021GL094,842.

Inan, U., H. Chang, R. Helliwell, W. Imhof, J. Reagan, and M. Walt (1985), Precipitation of radiation belt electrons by man-made waves: A comparison between theory and measurement, *J. Geophys. Res.*, *90*, 359.

Inan, U., T. Bell, J. Bortnik, and J. Albert (2003), Controlled precipitation of radiation belt electrons, *J. Geophys. Res.*, *108*, 1186, doi:10.1029/2002JA009580.

Karpman, V. I., Y. N. Istomin, and D. R. Shklyar (1974), Nonlinear theory of a quasimonochromatic whistler mode packet in inhomogeneous plasma, *Plasma Phys.*, *16*, 685.

Katoh, Y. (2014), A simulation study of the propagation of whistler-mode chorus in the Earth's inner magnetosphere., *Earth Planets Sp.*, *66*, doi:10.1186/1880–5981–66–6.

Kondrat'ev, I. G., A. V. Kudrin, and T. M. Zaboronkova (1999), *Electrodynamics of density ducts in magnetized plasmas*, Gordon and Breach, Amsterdam.

Kostrov, A. V., A. V. Kudrin, L. E. Kurina, G. A. Luchinin, A. A. Shaykin, and T. M. Zaboronkova (2000), Whistlers in thermally generated ducts with enhanced plasma density: exitation and propagation, *Phys. Scripta*, *62*, 51.

Liu, J., V. Angelopoulos, A. Runov, and X. Z. Zhou (2013), On the current sheets surrounding dipolarizing flux bundles in the magnetotail: The case for wedgelets, *J. Geophys. Res.: Space Phys.*, *118*, 2000.

Malykhin, A. Y., E. E. Grigorenko, D. R. Shklyar, E. V. Panov, O. L. Contel, L. Avanov, and B. Giles (2021), Characteristics of resonant electrons interacting with whistler waves in the nearest dipolarizing magnetotail, *J. Geophys. Res.: Space Phys.*, *126*, e2021JA029,440.

Nunn, D. (1974), A self-consistent theory of triggered vlf emissions, *Planet. Space Sci.*, *22*, 349.

Nunn, D., and A. J. Smith (1996), Numerical simulations of whistler-triggered vlf emissions observed in antarctica, *J. Geophys. Res.*, *101*, 5261.

Omura, Y., and D. Summers (2006), Dynamics of high-energy electrons interacting with whistler mode chorus emissions inthe magnetosphere, *J. Geophys. Res.*, *111*, A09,222, doi:10.1029/2006JA011600.

Omura, Y., D. Nunn, H. Matsumoto, and M. J. Rycroft (1991), A review of observational, theoretical and numerical studies of vlf triggered emissions, *J. Atmos. Terr. Phys.*, *53*, 351.

Runov, A., V. Angelopoulos, M. I. Sitnov, V. A. Sergeev, and J. P. M. J. Bonnell (2009), Themis observations of an earthward-propagating dipolarization front., *Geophys. Res. Lett.*, *36*, L14,106.

Russell, C. T., B. J. Anderson, W. Baumjohann, and et al (2016), The magnetospheric multiscale magnetometers, *Space Sci. Rev.*, *199*, 189.

Sazhin, S. (1993), *Whistler-mode waves in a hot plasma*, Cambridge University Press, Cambridge.

Sitnov, M. I., M. Swisdak, and A. V. Divin (2009), Dipolarization fronts as a signature of transient reconnection in the magnetotail, *J. of Geophys. Res.: Space Phys.*, *114*(A4).

Stenzel, R. (1976), Whistler wave propagation in a large magnetoplasma, *Phys. Fluids*, *19*, 857.

Stenzel, R. (1999), Whistler waves in space and laboratory plasma, *L. Geophys. Res.*, *104*, 14,379.

Storey, L. R. O. (1954), An investigation of whistling atmospheres, *Phil. Trans. Roy. Soc. London, A*, *246*, 113.

Streltsov, A. (2021a), Whistlers in the Plasmasphere, *J. Geophys. Res.: Space Phys.*, *126*, doi:10.1029/2020JA028933.

Streltsov, A. (2021b), Whistler on a Shelf, *J. Geophys. Res.: Space Phys.*, *126*, e2021JA029,403, doi:10.1029/2021JA029403.

Streltsov, A. V., M. Lampe, W. Manheimer, G. Ganguli, and G. Joyce (2006), Whistler propagation in inhomogeneous plasma, *J. Geophys. Res.*, *111*, doi: 10.1029/2005JA011357.

Torbert, R., C. T. Russell, W. Magnes, and et al. (2016), The fields instrument suite on mms: Scientific objectives, measurements, and data products, *Space Sci. Rev.*, *199*, 105.

Trakhtengerts, V., M. Rycroft, and A. Demekhov (1996), Interaction of noise-like and discrete ELF/VLF emissions generated by cyclotron interactions, *J. Geophys. Res.*, *101*, 13,293.

Trakhtengerts, V., M. Rycroft, D. Nunn, and A. Demekhov (2003), Cyclotron acceleration of radiation belt electrons by whistlers, *J. Geophys. Res.*, *108*, doi: 10.1029/2002JA009559.

Xu, X., L. Chen, C. Zhou, X. Liu, Z. Xia, J. Simpson, and Y. Zhang (2020), Two-dimensional full-wave simulationof whistler mode wave propagationnear the local lower hybrid resonance frequency in a dipolefield., *J. Geophys. Res.*, *125*, e2019JA027,750, doi:10.1029/2019JA027750.

Yin, Z. F., X. Z. Zhou, Q. G. Zong, Z. Y. Liu, C. Yue, and Y. Xiong (2021), Inner magnetospheric magnetic dips and energetic protons trapped therein: Multi-spacecraft observations and simulations, *Geophys. Res. Lett.*, *48*, e2021GL092,567.

Yu, X., and Z. Yuan (2022), Duct effect of magnetic structures on whistler waves, *J. Geophys. Res.*, *127*, doi:10.1029/2022JA031013.

Zhou, M., M. Ashour-Abdalla, X. Deng, D. Schriver, M. El-Alaoui, and Y. Pang (2009), Themis observation of multiple dipolarization fronts and associated wave characteristics in the near-earth magnetotail., *Geophys. Res. Lett.*, *36*.

Zudin, I., T. Zaboronkova, M. Gushchin, N. Aidakina, S. Korobkov, and C. Krafft (2019), Whistler waves' propagation in plasmas with systems of small-scaledensity irregularities: Numerical simulations and theory., *Radiophys. Quant. Electron.*, *124*, 4739, doi:10.1029/2019JA026637.

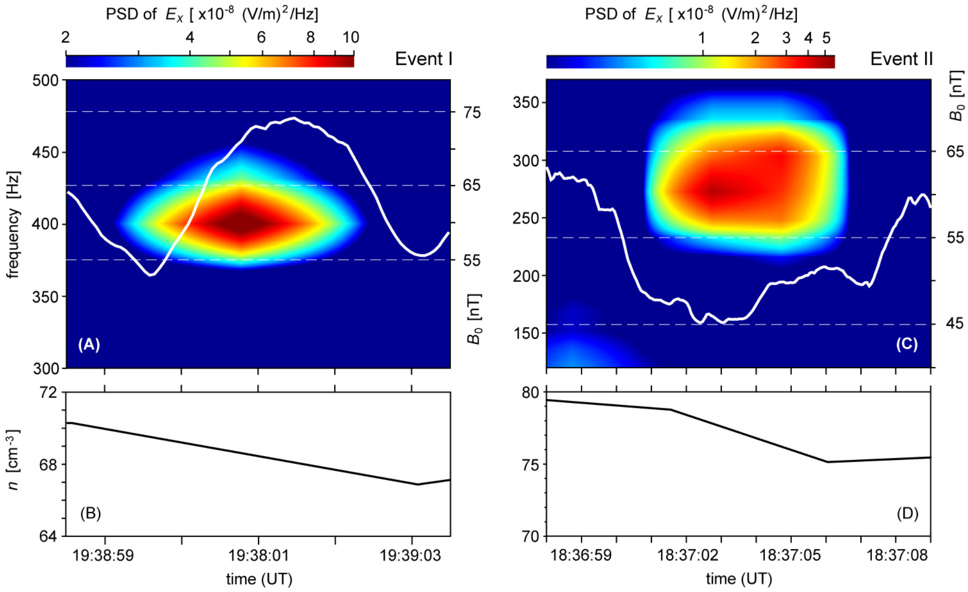

Figure 1. Two examples of the localized wave packets observed by the MMS1 satellite inside the high-B duct (Event I) and low-B duct (Event II) on 6 March 2016. Panels A and C show the Power Spectral Density (PSD) of E_x (color palette) and the background magnetic field (white line). Panels B and D show plots of the corresponding plasma density.

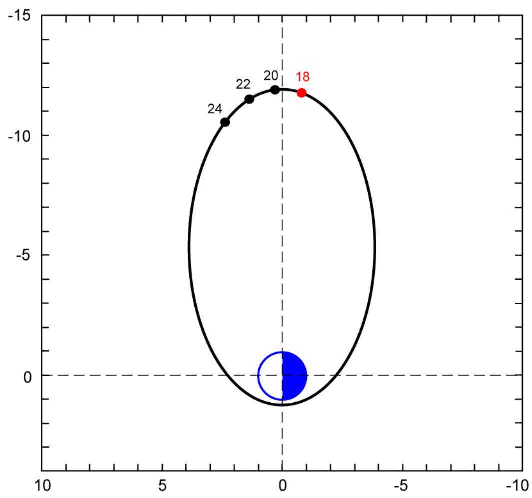

Figure 2. Trajectory and locations of MMS satellites in the GSE X-Y plane on March 6, 2016. The red dot marks the satellites location at 18:00 UT.

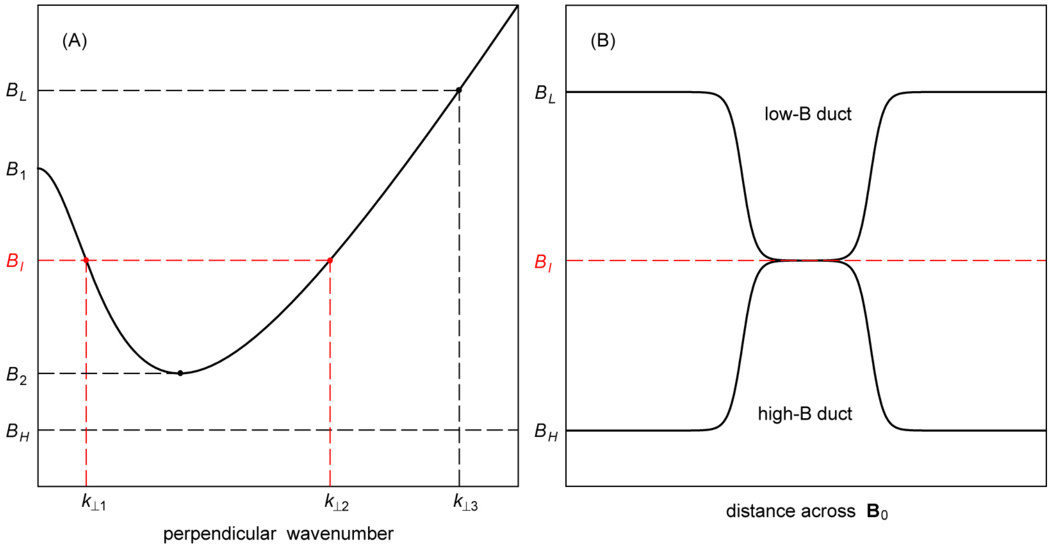

Figure 3. (A) Magnitude of the magnetic field vs the perpendicular wave number obtained as a solution of the dispersion relation (2) for $\omega = 1.71\times10^3$ rad/s ($f = 272$ Hz), $k_\parallel = 0.70$ rad/km ($\lambda_\parallel = 8.98$ km), and $\omega_{pe} = 4.98\times10^5$ rad/s ($n = 78$ cm^{-3}). (B) Magnitude of the magnetic field in the direction perpendicular to $\mathbf{B}_0$ corresponding to the low-B duct (LBD) and high-B duct (HBD).

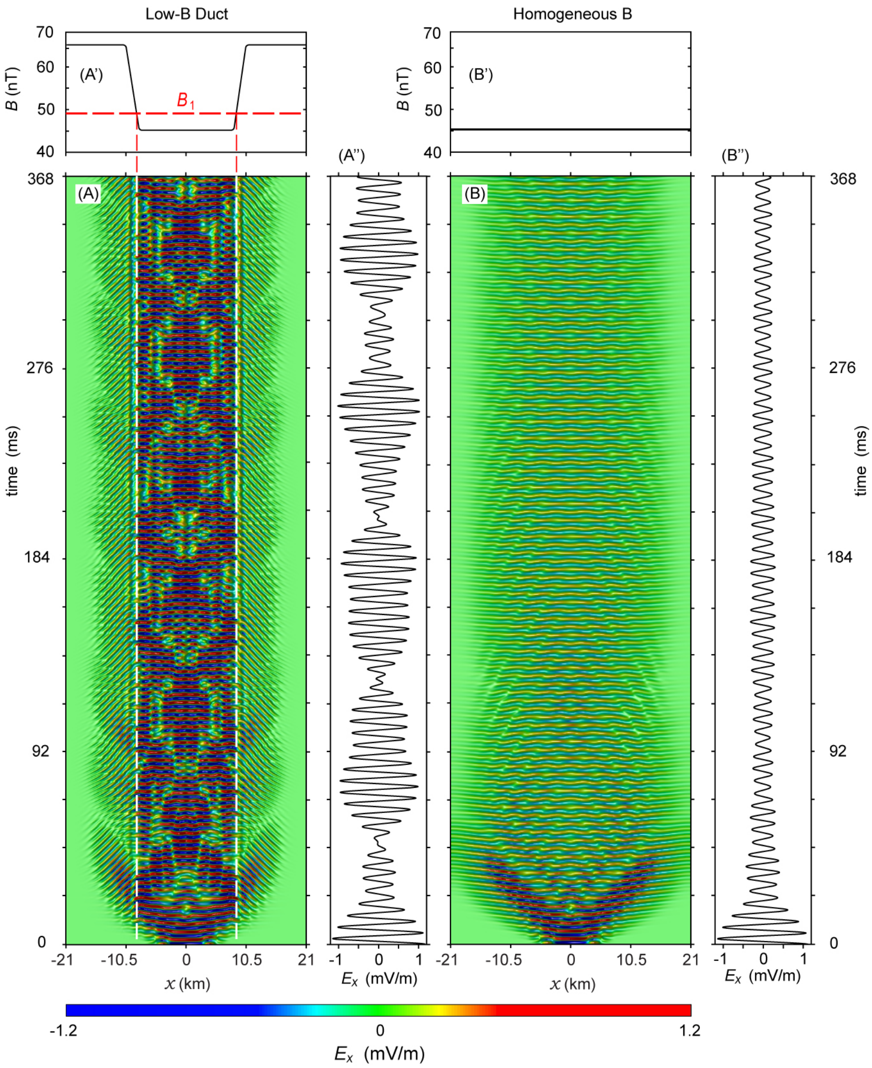

Figure 4. (A) Dynamics of E_x $(x,\, z = 0,\, t)$ in the simulation of the model low-B duct. The wave frequency is $f = 272$ Hz and $\lambda_{\|} = 7.70$ km. Plasma density is homogeneous across $\mathbf{B}_0$. (A') Profile of the magnetic filed across $\mathbf{B}_0$. (A") Dynamics of E_y at the center of the computational domain, E_x $(x = 0,\, z = 0,\, t)$. Panels (B), (B'), and (B") show results from the simulations with the homogeneous magnetic field, $B_0 = 45.4$ nT.

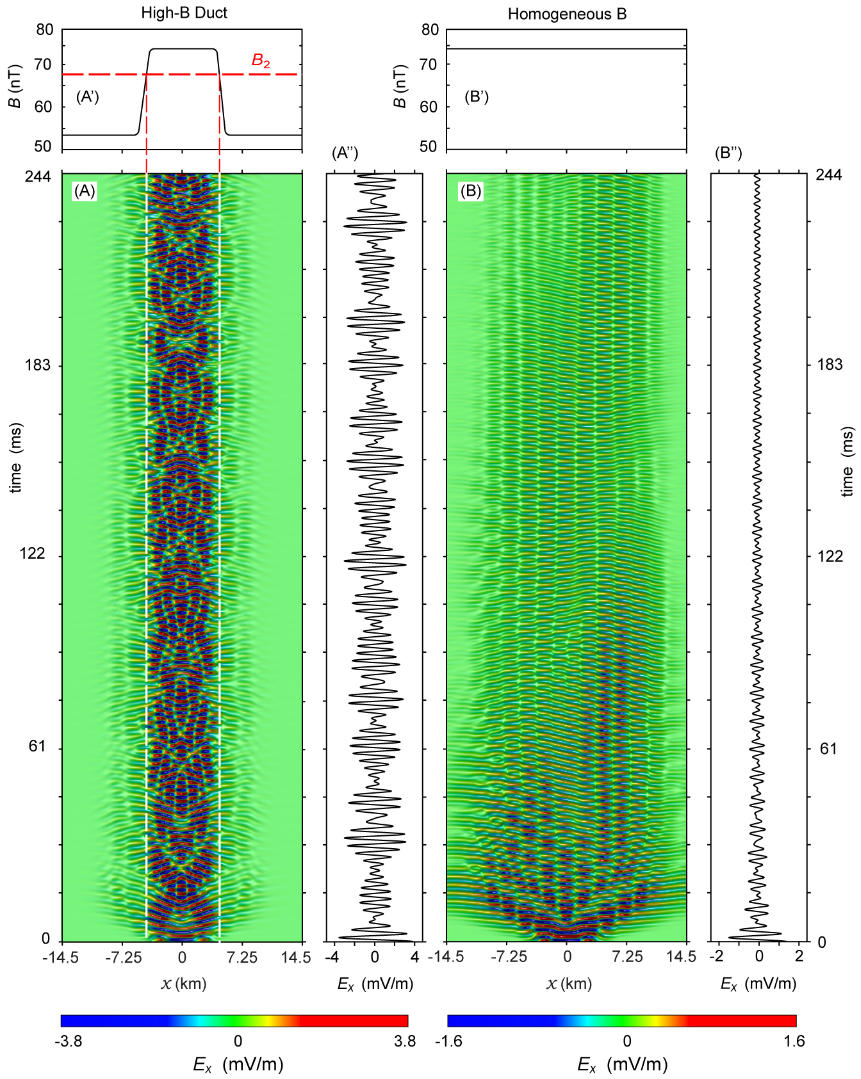

Figure 5. (A) Dynamics of E_x (x, $z = 0$, t) in the simulation of the model high-B duct. The wave frequency is $f = 410$ Hz and $\lambda_\parallel = 9.26$ km. Plasma density is homogeneous across $\mathbf{B}_0$. (A') Profile of the magnetic field across $\mathbf{B}_0$. (A") Dynamics of E_x at the center of the computational domain, E_x ($x = 0$, $z = 0$, t). Panels (B), (B'), and (B") show results from the simulations with homogeneous $B_0 = 74.0$ nT.

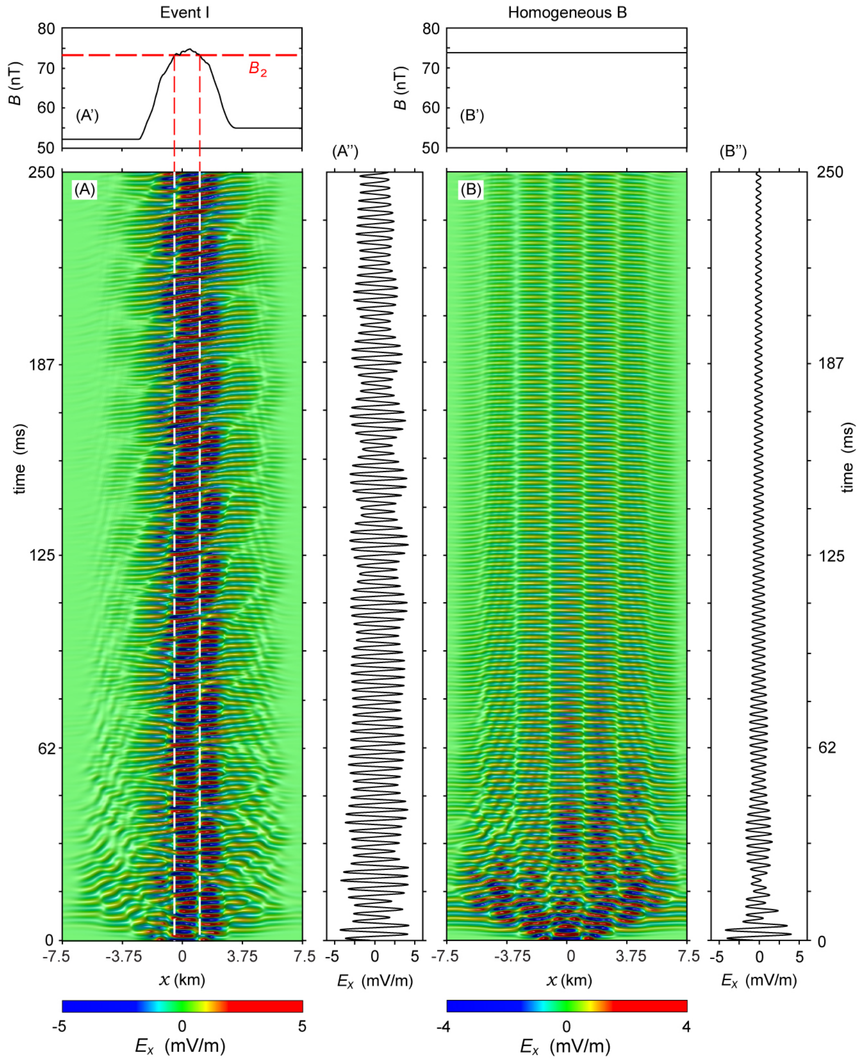

Figure 6. (A) Dynamics of E_x (x, $z = 0$, t) in the simulation with the parameters corresponding to the Event I. The frequency of the wave is $f = 400$ Hz and $\lambda_{\parallel} = 10.5$ km. (A') Profile of the magnetic field across $\mathbf{B}_0$. (A") Dynamics of E_x inside the low-B duct, E_x ($x = 0$, $z = 0$, t). Panels (B), (B'), and (B") show results from the simulations of the same wave in the plasma with the same density distribution and homogeneous $B_0 = 74.2$ nT.

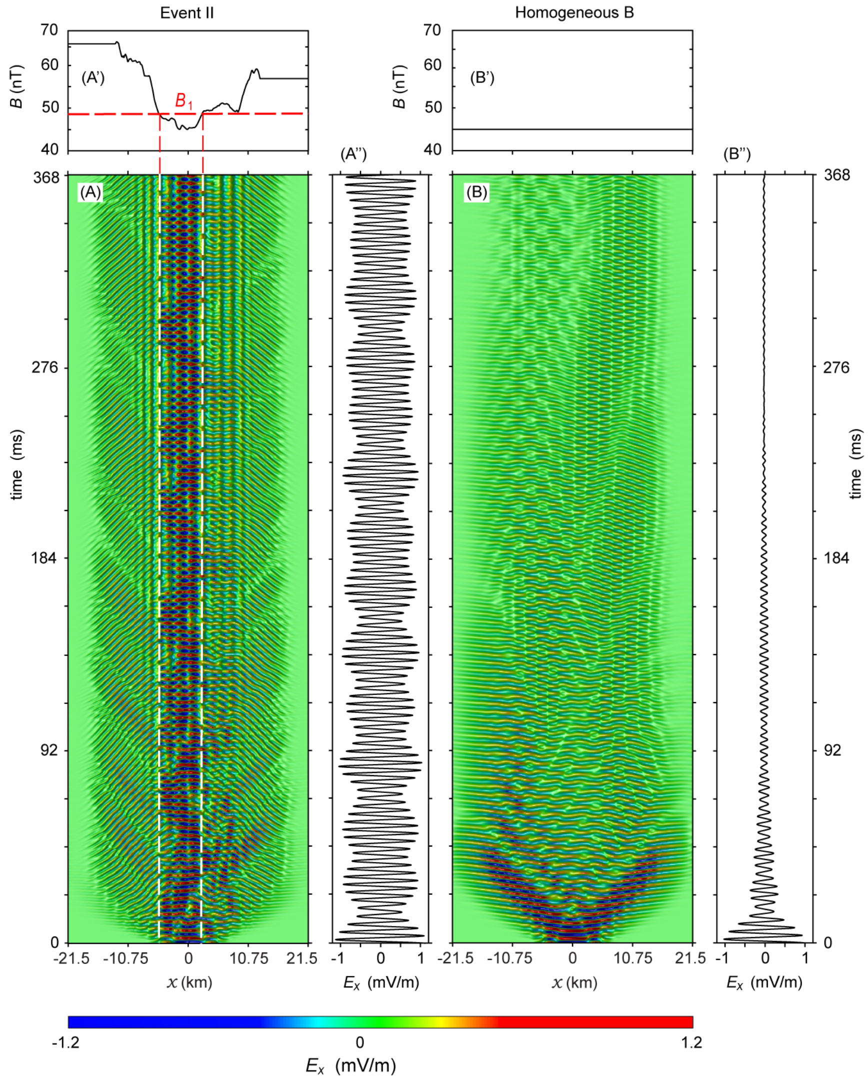

Figure 7. (A) Dynamics of E_x (x, z = 0, t) in the simulation with the parameters corresponding to the Event II. The frequency of the wave is f = 272 kHz and $\lambda_\parallel$ = 7.60 km. (A') Profile of the magnetic field across $\mathbf{B}_0$. (A") Dynamics of E_x inside the low-B duct, E_x (x = 0, z = 0, t). Panels (B), (B'), and (B") show results from the simulations of the same wave in the plasma with the same density distribution and homogeneous B_0 = 45.20 nT.